PCCP

Barrierless methane-to-methanol conversion: The unique mechanism of AlO+

Journal:	*Physical Chemistry Chemical Physics*
Manuscript ID	CP-ART-04-2020-002316.R1
Article Type:	Paper
Date Submitted by the Author:	29-May-2020
Complete List of Authors:	Sweeny, Brendan; Air Force Research Laboratory McDonald II, David; Air Force Research Laboratory Ard, Shaun; Air Force Research Laboratory, Space Vehicles Directorate; Boston College, Insitute of Scientific Research Viggiano, Albert; Air Force Research Laboratory, Space Vehicles Directorate Shuman, Nicholas; Air Force Research Laboratory,

Barrierless methane-to-methanol conversion: The unique mechanism of AlO^+

Brendan C. Sweeny,[1] David C. McDonald II,[1] Shaun G. Ard,[2] Albert A. Viggiano,[2] and Nicholas S. Shuman[2*]

1. *NRC postdoc at Air Force Research Laboratory, Space Vehicles Directorate, Kirtland Air Force Base, New Mexico 87117*
2. *Air Force Research Laboratory, Space Vehicles Directorate, Kirtland Air Force Base, New Mexico 87117*

* Corresponding author

Abstract

The kinetics of $AlO^+ + CH_4$ are studied from 300 – 500 K using a selected-ion flow tube. At all temperatures the reaction proceeds near the Langevin-Gioumousis-Stevenson collision rate with two product channels: hydrogen atom abstraction ($AlOH^+ + CH_3$, 86 ± 5 %) and methanol formation ($Al^+ + CH_3OH$, 14 ± 5%). Density functional calculations show the key Al-CH_3OH^+ intermediate is formed barrierlessly via a mechanism unique to aluminum, avoiding the rate-limiting step common to other MO^+. The reaction of $Al_2O_3^+ + CH_4$ follows a similar mechanism to that for AlO^+ through to the key intermediate; however, the conversion to methanol occurs only for AlO^+ due to favorable energetics attributed to a weaker Al^+-CH_3OH bond. Importantly, that bond strength may be tuned independent of competing product channels by altering the acidity of the Al with electron-withdrawing or donating groups, indicating a key design criteria to develop a real world Al-atom catalyst.

Introduction

Conversion of methane to methanol represents a promising approach to safely transporting fuels derived from methane, as well as being the rate-limiting step for numerous industrial chemical reactions.[1-3] There is currently no large-scale industrial process for activating the C-H bond of methane under ambient conditions. In the search for an effective catalyst, the fundamental reactivity of methane with a majority of the possible gas phase metal oxide cations, MO^+, have been studied either through experiment or calculation.[4-8] These results are summarized for the full periodic table in Figure 1. Most of the unstudied species are those where the oxide cation bond energy is very small (e.g. the alkali metals) such that experimental investigation is difficult, or very large (e.g. the lanthanides and actinides) where no reactivity is likely possible at thermal energies. In most cases reaction with methane results in hydrogen abstraction products, MOH^+ and a methyl radical, or oxygen transfer forming M^+ and CH_3OH. Activity with methane, in particular for methanol production, is most common for transition metals with greater than half-filled d-shells where the bond strength of MO^+ is not too large. These different MO^+ react with widely varying rate constants and product branching fractions, controlled by the relative energetics of transition states and reaction products, but generally through a common mechanism.[5]

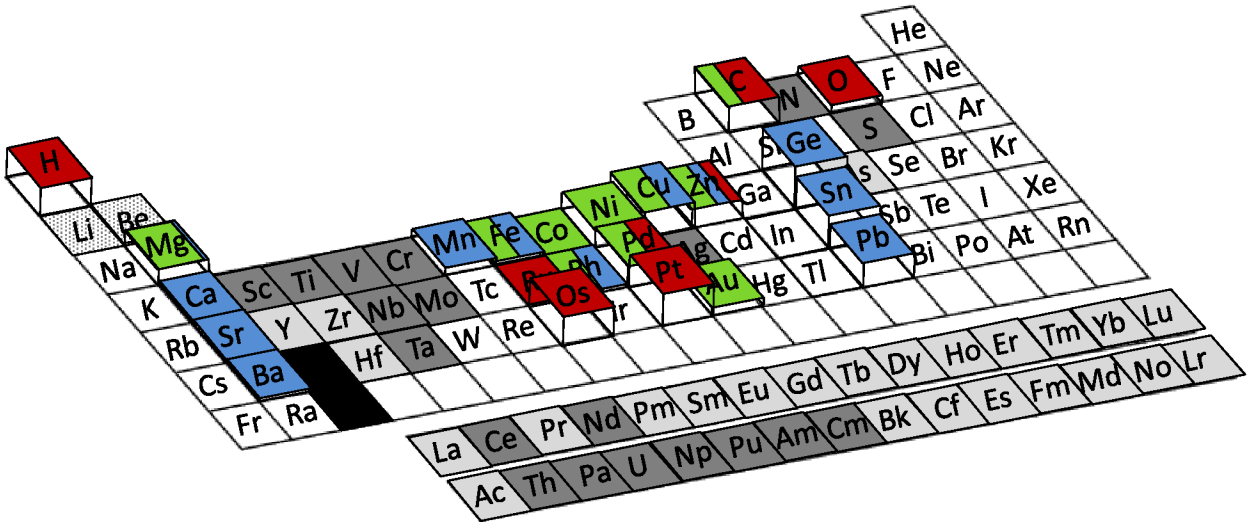

Figure 1. Graphical summary of reactivity of $AO^+ + CH_4$ at thermal energies where A is an atom. The height of each element indicates the reaction rate constant on a linear scale, with the largest values being ~10^{-9} cm^3 s^{-1}. The colors of each element indicate the product channels and branching fractions (green = $A^+ + CH_3OH$, blue = $AOH^+ + CH3$, red = other reactivity (e.g. $ACH_2^+ + H_2O$), dark grey = no reaction, light grey = unstudied but endothermic to methanol production, dotted = investigated by calculations without detailed reaction predictions, white = unstudied by experiment or theory).

Data on reactivity of Group 13 metal oxide cations with methane is notably absent from the literature. The oxide affinities of the Group 13 cations decrease down the periodic table, such that it is difficult to perform experiments on this group for GaO^+ or heavier, but surprisingly AlO^+, which is bound by about 1.50 eV,[9] has not been reacted with CH_4. Indeed the literature contains almost no AlO^+ chemistry, with recent work on its atmospheric implications[10] being the exception.

Here, we investigate the kinetics of AlO^+ with CH_4 using a variable-temperature selected ion flow tube and the mechanism with quantum chemical calculations. This allows us to elucidate the elementary steps of this reaction mechanism. Understanding the underlying mechanism for C-H bond activation as well as the factors controlling product selectivity is important to designing catalysts for industrial use and using earth-abundant and cost-effective materials is important for the commercial viability of any catalyst. The combined approach allows us to understand 1) how this system produces methanol through a barrierless mechanism unique to aluminum or possibly Group 13 species, 2) why the analogous $Al_2O_3^+$ reaction, which follows the same mechanism to access the critical intermediate, does not produce methanol, and 3) how to tune the key molecular parameter enabling methanol production.

Methods

Temperature dependent kinetics measurements were conducted using a variable-ion source temperature-adjustable selected-ion flow tube described in detail elsewhere.[11] AlO^+ was formed using a Smalley-type laser vaporization source[12] with a ¼" diameter, rotating, translating Al rod (99.9%, ESPI Metals) as the target. Perpendicular to the Al rod and laser (Nd: YAG, 532 nm, 100 Hz, 3-5 mJ/pulse, Litron) path, an expansion of dynamically mixed 100 std. cm^3 min^{-1} Ar and 20 std. cm^3 min^{-1} O_2 was introduced using a pulsed valve (Parker) with a 1 mm aperture operating at 100 Hz. Generated ions were

transported using a series of rectilinear quadrupole ion guides and quadrupole bender to a quadrupole mass filter. Mass-selected ions were injected into a 1-m long, 7 cm diameter stainless steel flow tube via a Venturi inlet. The flow tube wall temperature was held at 300, 400, or 500 K by means of resistive heating elements. The flow tube pressure was maintained at 0.33 Torr using a He buffer gas. The reactant gas, CH_4 (99.999% Matheson), was introduced using a mass flow meter (MKS) 59 cm from the end of the flow tube allowing for a typical reaction time of 2.5 ms. At the terminus of the flow tube, the buffer gas was evacuated using a roots pump and the center axis of the flow sampled through a 4 mm aperture into a differentially pumped region. Sampled ions were transported using a rectilinear quadrupole ion guide to the entrance of an orthogonally-accelerated time-of-flight mass spectrometer for mass analysis. Relative ion concentrations were measured as a function of CH_4 concentration, and kinetics derived using well-established methods.[13]

Upon injection into the flow tube, reactant ions undergo $10^4 - 10^5$ collisions with the helium buffer gas. While this is sufficient to thermalize polyatomic ions to the temperature of the flow tube wall, thermalization of electronic states of atomic and diatomic species lacking low-energy vibrational modes is less certain. Here, AlO^+ primary ions reacting with methane decay following a single exponential; however, this does not preclude multiple initial states reacting at the same rate, in this case at the LGS collisional limit. All kinetics data, including product branching fractions, was consistent from day-to-day and under different source conditions (e.g. laser power), suggesting the distribution was thermalized in that producing such a consistent excited distribution was unlikely. AlO^+ in particular has low lying excited states, with triplet states calculated to be only a few hundred wavenumbers above a singlet ground state.[14, 15] That the states are separated by energies similar to thermal translational energies may enable thermalization in this case.

Stationary points along the reaction coordinate were optimized at B3LYP/TZVP[16] and at B2PLYP/def2-TZVP[17], and single point energies calculated at CCSD(T)/aug-cc-pvtz//B2PLYP/def2TZVP using Gaussian 09.[18] Reported energies are zero-point corrected using unscaled harmonic frequencies. The nature of intermediates and transition states was confirmed by the presence of 0 or 1 imaginary frequency. Pathways between stationary points were confirmed by intrinsic reaction coordinate (IRC) calculations. Open-shell species were calculated using unrestricted methods and were evaluated for spin contamination and wavefunction instability. The region including the crossing seam was identified by calculating energies for the corresponding singlet complexes from the structures along the triplet transition state IRC.

Results and Discussion

AlO^+ reacts efficiently with CH_4 from 300 – 500 K. The measured rate constant of $9.8 \pm 2.5 \times 10^{-10}$ $cm^3\ s^{-1}$ (Figure 2) is within error of the Langevin-Gioumousis-Stevenson (LGS) collision rate of 1.1×10^{-9} $cm^3\ s^{-1}$.[19] At all temperatures studied, two primary product channels were observed, $AlOH^+ + CH_3$ and $Al^+ + CH_3OH$. $AlOH^+$ was the majority product at 86% ± 5%, with $Al^+ + CH_3OH$ resulting from 14% ± 5% (Figure 2). Neither the overall rate constant nor the product branching changed significantly with temperature (Figure 2).

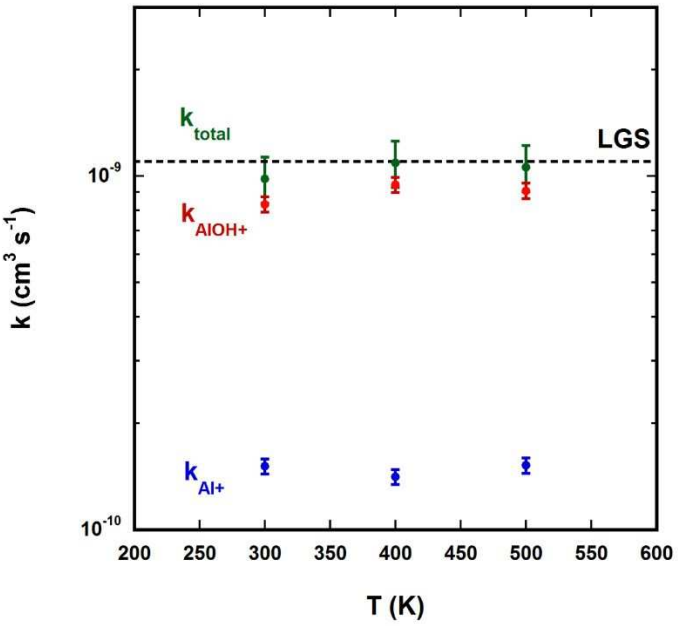

Figure 2. Total (green circles) and partial ($AlOH^+ + CH_3$, red circles; $Al^+ + CH_3OH$, blue circles) rate constants for $AlO^+ + CH_4$ as a function of temperature. The LGS collision rate[19] is indicated by a dashed line at 1.10×10^{-9} cm^3 s^{-1}.

Stationary points calculated along the reaction coordinate illustrate two accessible spin multiplicities (Figure 3). Little variation in equilibrium geometries was found between the hybrid B3LYP functional and the double hybrid B2PLYP method, with the exception of $AlOH^+$. B3LYP predicts a "bent" $AlOH^+$ geometry with both the TZVP and larger def2-TZVP basis sets, as do several other DFT functionals (TPSS0, TPSSh, M06L), while MP2, B2PLYP, the M06 functional, and a full optimization at CCSD(T)/aug-cc-pvtz all predict a linear equilibrium geometry. Energies differed from CCSD(T) by unsigned means of 0.25 eV for B3LYP and 0.09 for B2PLYP, with maximum deviations of 0.49 and 0.31 eV respectively. The deviations were not uniformly distributed about zero, with no B3LYP or B2PLYP energy being more than 0.04 eV lower than the CCSD(T) energy. The calculations well-reproduce product exothermicities from experiment[9, 20, 21] and multireference calculations.[22] Uncertainties in the modest B3LYP calculated energies approaching 0.5 eV would not be unexpected,[23] with smaller uncertainties in the higher level calculations. The present calculations find that the ground state of AlO^+ is a triplet with the excited singlet state +0.06 eV higher; however, the actual multiplicity of ground state AlO^+ is of some debate. Complete active space (CASSCF) calculations[24] suggest a triplet ground state while multi-reference configuration interaction (MRCI) calculations[14, 15, 25] suggest a singlet ground state with the triplet ~0.05 eV higher.

$^3AlO^+$ reacting with CH_4 forms an entrance complex (INT1) lying -0.7 eV below reactants but only -0.2 eV below transition state TS1, resulting in a necessarily short lifetime. Upon quickly traversing TS1, the reaction enters a "bumpy" region of the potential (see Figure S2); only the lowest energy intermediate -1.8 eV below reactant energies (INT2*) is shown in Figure 3 for simplicity. On the triplet surface, dissociation into $^3Al^+ + CH_3OH$ is energetically inaccessible, lying 2.31 ± 0.15 eV[9, 26, 27] above reactant energies, which is reasonably consistent with 2.17 eV (1.86 eV) calculated using B2PLYP (CCSD(T)). Instead, dissociation into $^2AlOH^+ + {}^2CH_3$, ~ -1.3 eV below reactants (Figure 3), occurs

readily with a lifetime from INT2* to dissociation calculated assuming statistical behavior using orbiting transition state-phase space theory to be $t < 10^{-13}$ s. In the region between TS1 and INT2* the reaction may undergo intersystem crossing (ISC) to the singlet surface at CP forming INT3, the intermediate formed directly as an entrance complex from singlet $^1AlO^+ + CH_4$. ISC would need to occur on a timescale shorter than the lifetime of INT2*, and it is unclear if such a fast crossing is physically reasonable. On the singlet surface, dissociation to both $^1Al^+ + {}^1CH_3OH$ at -2.32 ±0.15 eV[9, 26] (-2.44 eV, B2PLYP; -2.64 eV, CCSD(T)) and $^2AlOH^+ + {}^2CH_3$ are then energetically accessible, and the experimental observation of $^1Al^+$ indicates that at least some fraction of reactions occur on the singlet surface.

Whether the reaction initiates on the singlet or a triplet surface, the observed large total rate constant is consistent with the calculated reaction coordinates. In both cases the short range potential is sufficiently low in energy throughout the reaction that dissociation back to reactants will not be competitive. Instead, the reaction rate is determined by the long-range potential (i.e. capture-controlled), and the agreement with the LGS capture rate constant indicates little to no anisotropy in that potential, which would reduce the rate below that value.

Assuming a ground state $^3AlO^+$ as calculated here, the experimental product branching fractions can be rationalized either of two ways: at least ~14% of systems may undergo ISC to the singlet surface, or $^1AlO^+$ may lie only slightly above $^3AlO^+$, by ~0.02 eV, such that 14 and 18% of the equilibrium population are singlets from 300 and 500 K, respectively. It is worthwhile to note if the ISC occurs it must be efficient, as the competing lifetime for formation of the hydrogen atom transfer (HAT) product is only $\sim 10^{-13}$ s. Alternatively assuming a singlet $^1AlO^+$ ground state, the observed product branching must be controlled by the competition between the two dissociations from INT3. Statistical treatment suggests a lifetime in this intermediate of a few ps, and it is reasonable but not certain that intramolecular vibrational energy redistribution is largely complete prior to dissociation. Surprisingly, while the $Al^+ + CH_3OH$ channel is energetically favored by more than 1 eV, the entropic preference of the $AlOH^+ + CH_3$ channel (due to added rotations) suggests the channels are competitive in the energy range corresponding to thermal $AlO^+ + CH_4$ (Figure 4).

To understand this result, it is important to recognize that while the reactants here are at thermal energies, intermediate complexes are sampled at energies well above their minima; i.e. they are highly excited. The INT3 complex is sampled with ~4 eV of internal energy, allowing the entropic advantage of the $AlOH^+$ product channel to overcome the energetic advantage of the Al^+ channel. Rate curves for both channels are calculated assuming orbiting transition state phase-space theory (PST),[28, 29] with the larger number of rotational modes in the $AlOH^+ + CH_3$ products driving the steeper increase in rate constant with energy. The uncertainties in these *a priori* rate curves are necessarily large due to uncertainty in the dissociation thresholds, calculated frequencies, and contributions of anisotropy in the potentials reducing the curves below the PST limit. Under statistical assumptions, without adjustment to the calculated energies, the experimental rate constants and product branching fractions across the temperature range are well-modeled by assuming all reactions occurring solely on the singlet surface. The reaction is modeled to occur at the Langevin-Gioumousis-Stevenson collisional rate at all temperatures. The modeling shows 10% branching to Al^+ at 300 K trending minimally to 9.5% at 500 K; details of such modeling have been presented previously.[30] While this is a compelling result, we emphasize that the uncertainties in the modeling do not rule out that some fraction of the $AlOH^+$ product is formed from dissociation on the triplet surface.

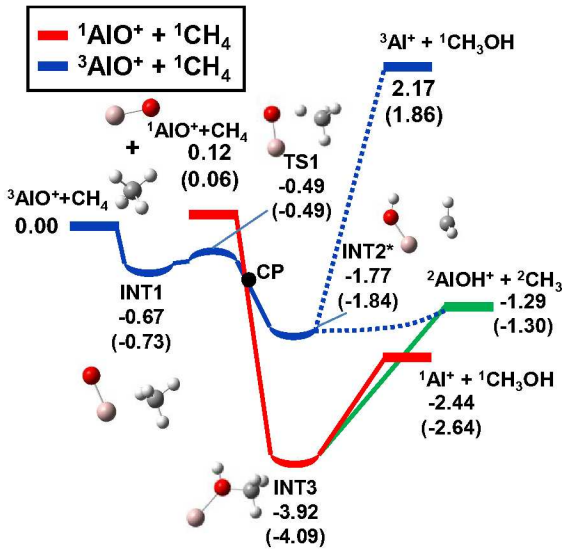

Figure 3. Simplified reaction coordinate of $AlO^+ + CH_4$. Dashed lines indicate shallow stationary points omitted for brevity (see Figure S2 for a more complete description). Zero-point corrected energies relative to $^3AlO^+ + {}^1CH_4$ calculated at the B2PLYP/def2tzvp and CCSD(T)/aug-cc-pvtz//B2PLYP/def2tzvp (in parentheses) are indicated in electron volts.

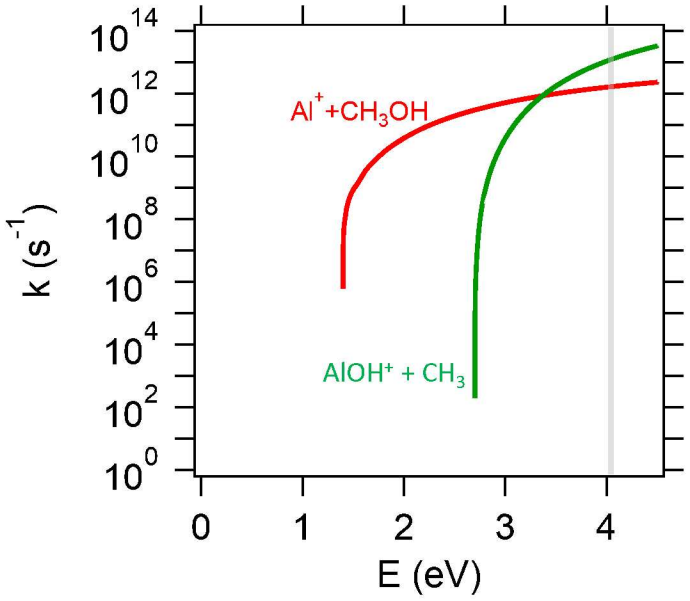

Figure 4. Calculated unimolecular rate curves for dissociation from $^1AlCH_3OH^+$ to $Al^+ + CH_3OH$ (red) and $AlOH^+ + CH_3$ (green) as a function of energy relative to the bottom of the $^1AlCH_3OH$ well for J=60 (the peak of orbital angular momentum distribution for $AlO^+ + CH_4$ at 300 K, although the curves show little J-dependence for J < 100). Energies sampled in the present experiment, corresponding to the energy of $AlO^+ + CH_4$ are indicated by the grey, shaded region.

The calculated minimum energy path on the triplet surface $^3AlO^+$ and CH_4 is similar to other MO^+ species undergoing HAT with methane.[5] $^3AlO^+$ has spin density on the O atom (Figure S3), similar to $Al_2O_3^+$, MgO^+, and CuO^+, and studies of these systems have indicated this increased spin density on the oxygen as a prerequisite for HAT.[31] Examination of the spin density and spin natural orbitals of ^{3}TS1 indicates a primarily HAT mechanism (Figures S4, S5, and Table S3). Further, the deformation energy[5] is nearly 1:1 with the barrier height, indicative of a HAT, as opposed to a proton-coupled electron transfer, mechanism. In the present case, the energetics suggest this channel occurs rapidly in a non-statistical manner, presumably at long range.

However, the mechanism to produce CH_3OH on the $^1AlO^+$ potential surface (directly or after ISC) is distinct from that of other metal oxide cations. Previously studied MO^+, including transition metals as well as MgO^+ follow the typical mechanism illustrated in Figure 5. $MO(H)CH_3^+$ (INT3) is formed stepwise through two additional intermediates, with an initial transition state (TS1) inserting MO^+ into a C-H bond generally being rate-limiting.[32] The overall rate of the reaction is controlled by the energy of TS1. Product branching to $M^+ + CH_3OH$ or $MOH^+ + CH_3$ is controlled by the relative energetics of those product channels in addition to the energy of TS2, a methyl migration. Many of the MO^+ systems involve more than one spin surface and one or more ISC may be involved in the reaction as well.

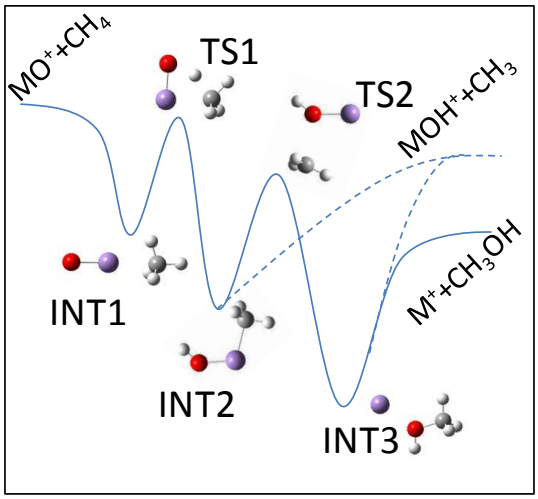

Figure 5. Cartoon of the reaction coordinate typical for $MO^+ + CH_4$ where M is a 1st row transition metal.

The present reaction instead follows a mechanism similar to that previously detailed for $Al_2O_3^+ + CH_4$,[33] whereby INT3 Al-O(H)CH_3^+ (or AlO_2Al-O(H)CH_3^+) complex is formed directly with no energetic barriers or additional intermediates (Figure 6). The intrinsic reaction coordinate is calculated starting from a geometry corresponding to $AlO^+ + CH_4$ with 4.0 Å between the O and C atoms and terminates at INT3 in Figure 3. An attractive potential orients the methane such that O-H-C is roughly in a linear geometry as the CH_4 approaches AlO^+. At $r_{C\text{-}O}$ = 2.8 Å, a sudden hydrogen atom transfer from the C atom to the O atom occurs, significantly stabilizing the complex to ~1.5 eV below the energy of the separated reactants. At this same point, the CH_3 group transitions toward the D_{3h} geometry of the methyl radical.

The Al-O-H angle slowly bends from roughly linear to about 100°. Finally, the O atom is pulled slightly away from the Al atom and toward the C atom, the CH_3 group returns to a C_{3v} geometry, and Al^+-CH_3OH is formed.

Like other MO^+ species, the mechanism begins with AlO^+ abstracting a hydrogen atom (i.e. TS1 in Figure 5), but then differs in that there is no insertion of MO into the C-H bond and, because the inserted complex (INT2 in Figure 5) is never formed, the methyl migration (TS2 in Figure 5) is also avoided. The reaction coordinate is qualitatively similar when calculated using a range of basis sets (TZVP, def2-TZVP, 6-311+G(d)), functionals (B3LYP, TPSS0, M06, CAMB3LYP), or with MP2. This direct mechanism is only observed on the singlet $AlO^+ + CH_4$ surface. This behavior, avoiding the common rate-limiting step to methane activation, is seemingly unique to aluminum and possibly the other species in the Group 13 period (similar reaction coordinates are calculated for BO^+, GaO^+, and InO^+).

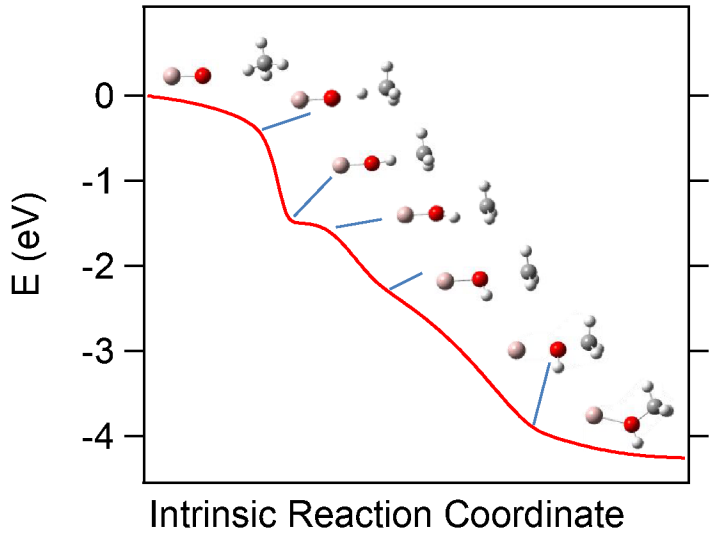

Figure 6. Intrinsic reaction coordinate for the approach of $^1AlO^+ + CH_4$ calculated at the B2PLYP/def2TZVP level. Structures denote inflection points along the reaction coordinate are shown.

The $Al_2O_3^+ + CH_4$ reaction forms the key intermediate (AlO_2Al^+-$O(H)CH_3$) analogous to INT3 in Figure 3, but does not form methanol at thermal energies.[33] While the product channel is exothermic, the AlO_2Al^+-$O(H)CH_3$ bond dissociation energy (BDE) is large (2.8 eV) and competing channels dominate. The Al^+-$O(H)CH_3$ bond here is much weaker, 1.6 eV, allowing for competitive methanol production. The environment of the Al-atom therefore affects the BDE, which in turn controls methanol production.

Schwarz and co-workers have shown that ligating a metal oxide species can drastically affect the mechanism and selectivity of methane activation, and that those same effects can be achieved by simulating the electric field of a negative point charge.[34, 35] In the present system, the Al^+ and $-O(H)CH_3$ act as a Lewis acid/base pair with the electrophilicity of the Al^+ atom determining the Al^+-$O(H)CH_3$ BDE. A less electrophilic Al atom results in a weaker Al^+-$O(H)CH_3$ bond and a more competitive $Al^+ + CH_3OH$ product channel. The $Al_2O_3^+$ species maintains a more positive partial charge on the Al binding site than

found in AlO^+, resulting in more electron-withdrawing character and a stronger Al^+-$O(H)CH_3$ bond. To confirm this behavior, BDE's of $[R\text{-}Al\text{-}O(H)CH_3]^+$ were calculated for various donating/withdrawing ligands (Figure 7 and Table S1), showing a direct relationship between the magnitude of the partial positive charge on the Al atom as a result of the attached ligand and the resulting Al^+-$O(H)CH_3$ BDE. Notably the competing R-$AlO(H)^+$-CH_3 BDE is more constant with R and does not show such a strong correlation. Addition of an electron withdrawing ligand should lower the RAl^+-CH_3OH BDE without having a commensurate effect on the competing dissociation, thereby favoring methanol production. This behavior provides a control to tune for or against methanol production. For instance, $Al_2O_3^+ + CH_4$ does not form methanol despite readily forming the $[AlO_2AlO(H)CH_3]^+$ complex because the bridging oxygen atoms are strongly electron withdrawing, precluding dissociation at the RAl^+-CH_3OH bond.

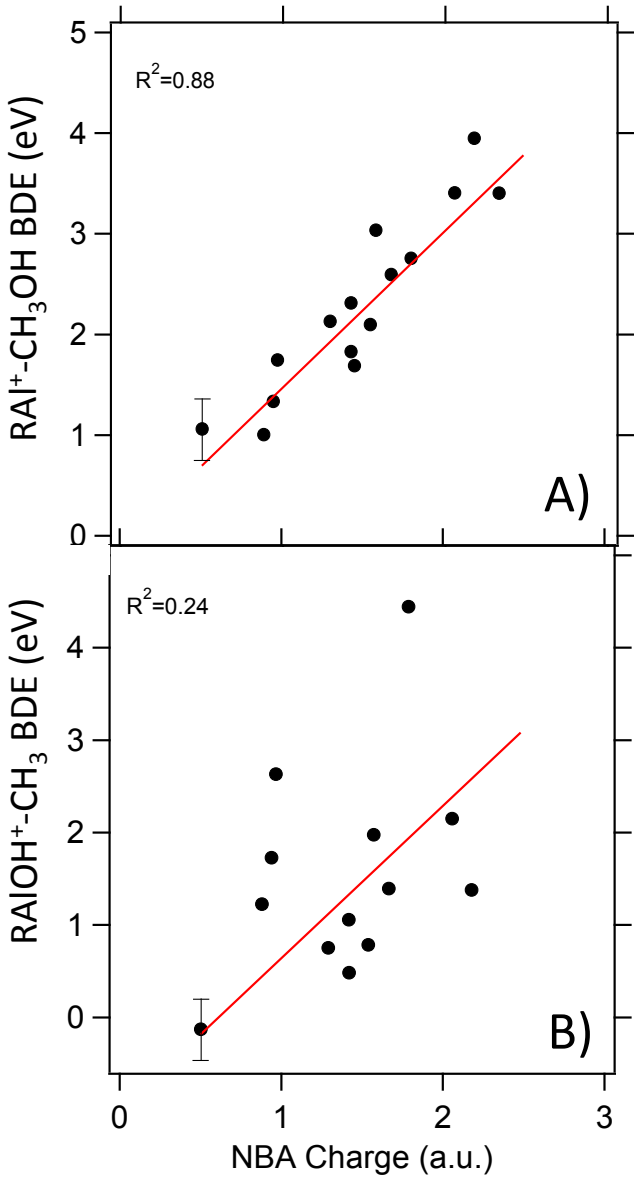

Figure 7. 0 K bond dissociation energies calculated at the B2PLYP/def2TZVP level as a function of natural bond analysis partial charge on the Al-atom for various ligands R in $RAl\text{-}O(H)CH_3^+$ for A) The

RAl^+-CH_3OH BDE and B) the competing $RAlOH^+$-CH_3 BDE. Estimated uncertainty in the calculated values is shown. Details of the ligands R are provided in Table S1.

Analogous to ligands affecting the reactivity in these gas-phase studies, single-atom catalysts offer tunability of active species through selection of the support.[36, 37] While little literature exists on single aluminum atom catalysts, the present gas-phase results suggest aluminum atoms dispersed on or singly doped[38] into an electron-donating support, such as MgO, is a promising route to methane-to-methanol conversion. The same electron-donating environment that enables CH_3OH to easily leave as a product also lowers the oxygen affinity of the active aluminum narrowing the energetic window of a possible catalytic cycle, but the gas-phase results here suggest such a window does exist.

Conclusion

The kinetics of $AlO^+ + CH_4$ have been measured using a selected-ion flow tube apparatus under thermal conditions from 300 – 500 K. The reaction proceeds near the LGS collisional rate yielding ~85% $AlOH^+$ and ~15% Al^+ at all temperatures. The Al^+ product channel corresponds to activation of CH_4 to CH_3OH. The calculated reaction coordinate suggests a mechanism where the Al-CH_3OH^+ intermediate, key for methanol production, is formed directly without a barrier, distinct from other $MO^+ + CH_4$ systems where the analogous intermediate is formed in a step-wise manner involving a rate-limiting transition state. Analogous direct formation of the key intermediate in the $Al_2O_3^+ + CH_4$ system has been previously noted; however, that reaction does not produce methanol. The AlO^+ and $Al_2O_3^+$ systems differ in that the RAl^+-CH_3OH bond energy is much lower (1.6 eV vs 2.8 eV) in the former, allowing for the methanol channel to compete with other product channels. Through calculation of bond energies of RAl^+-CH_3OH for various ligands R, it is shown that Al^+ and CH_3OH bond as a Lewis acid/base pair, and the bond strength may be increased or decreased by addition of electron withdrawing or donating ligands. We suggest that an analogous effect may be possible by selection of an electron-donating support for a single atom Al catalyst towards methane-to-methanol conversion.

Acknowledgements

This work was supported by the Air Force Office of Scientific Research under grant AFOSR-19RVCOR042. SGA performed part of this work under contract with the Boston College Institute for Scientific Research. BCS and DCM are supported through the National Research Council Research Advisory Program.

References

1. J. H. Lunsford, *Catal. Today*, 2000, **63**, 165-174.
2. A. Holmen, *Catal. Today*, 2009, **142**, 2-8.
3. P. Tang, Q. Zhu, Z. Wu and D. Ma, *Energy Environ. Sci.*, 2014, **7**, 2580-2591.
4. H. Schwarz, S. Shaik and J. Li, *J. Am. Chem. Soc.*, 2017, **139**, 17201.
5. J. Li, S. Zhou, J. Zhang, M. Schlangen, D. Usharani, S. Shaik and H. Schwarz, *J. Am. Chem. Soc.*, 2016, **138**, 11368-11377.
6. N. Dietl, C. van der Linde, M. Schlangen, M. K. Beyer and H. Schwarz, *Angew. Chem., Int. Ed. Engl.*, 2011, **50**, 4966-4969.
7. A. Bozovic, S. Feil, G. K. Koyanagi, A. A. Viggiano, X. H. Zhang, M. Schlangen, H. Schwarz and D. K. Bohme, *Chem. - Eur. J.*, 2010, **16**, 11605-11610.
8. J. Roithova and D. Schroder, *Chem. Rev.*, 2010, **110**, 1170-1211.
9. D. E. Clemmer, M. E. Weber and P. B. Armentrout, *J. Phys. Chem.*, 1992, **96**, 10888-10893.
10. S. M. Daly, D. L. Bones and J. M. C. Plane, *Phys. Chem. Chem. Phys.*, 2019, **21**, 14080-14089.
11. B. C. Sweeny, S. G. Ard, A. A. Viggiano and N. S. Shuman, *J. Phys. Chem. A*, 2019, **123**, 4817-4824.
12. M. A. Duncan, *Rev. Sci. Instrum.*, 2012, **83**, 041101.
13. C. J. Howard, *J. Phys. Chem.*, 1979, **83**, 3-9.
14. P. Yan, X. Yuan, S. Yin, X. Liu, H. Xu and B. Yan, *Comput. Theor. Chem.*, 2017, **1117**, 258-265.
15. O. Sghaier, R. Linguerri, M. M. A. Mogren, J. S. Francisco and M. Hochlaf, *Astrophys. J.*, 2016, **826**, 163.
16. A. Schäfer, C. Huber and R. Ahlrichs, *J. Chem. Phys*, 1994, **100**, 5829-5835.
17. F. Weigend and R. Ahlrichs, *Phys. Chem. Chem. Phys*, 2005, **7**, 3297-3305.
18. M. J. Frisch, G. W. Trucks, H. B. Schlegel, G. E. Scuseria, M. A. Robb, J. R. Cheeseman, G. Scalmani, V. Barone, B. Mennucci, G. A. Petersson, H. Nakatsuji, M. Caricato, X. Li, H. P. Hratchian, A. F. Izmaylov, J. Bloino, G. Zheng, J. L. Sonnenberg, M. Had, M. Ehara, K. Toyota, R. Fukuda, J. Hasegawa, M. Ishida, T. Nakajima, Y. Honda, O. Kitao, H. Nakai, T. Vreven, J. J. A. Montgomery, J. E. Peralta, F. Ogliaro, M. Bearpark, J. J. Heyd, E. Brothers, K. N. Kudin, V. N. Staroverov, R. Kobayashi, J. Normand, K. Raghavachari, A. Rendell, J. C. Burant, S. S. Iyengar, J. Tomasi, M. Cossi, N. Rega, J. M. Millam, M. Klene, J. E. Knox, J. B. Cross, V. Bakken, C. Adamo, J. Jaramillo, R. Gomperts, R. E. Stratmann, O. Yazyev, A. J. Austin, R. Cammi, C. Pomelli, J. W. Ochterski, R. L. Martin, K. Morokuma, V. G. Zakrzewski, G. A. Voth, P. Salvador, J. J. Dannenberg, S. Dapprich, A. D. Daniels, O. Farkas, J. B. Foresman, J. V. Ortiz, J. Cioslowski and D. J. Fox, GAUSSIAN 09 (Revision A.02), Gaussian Inc., Wallingford, CT, 2009.
19. G. Gioumousis and D. P. Stevenson, *J. Chem. Phys.*, 1958, **29**, 294-299.
20. J. S. Pilgrim, D. L. Robbins and M. A. Duncan, *Chem. Phys. Lett.*, 1993, **202**, 203-208.
21. P. J. Linstrom and W. G. Mallard, eds., *NIST Chemistry WebBook, NIST Standard Reference Database Number 69*, National Institute of Standards and Technology, Gaithersburg MD, 20899.
22. G. Chambaud, P. R. M. L. S. Palmieri and P, *Mol. Phys.*, 1997, **92**, 399-408.
23. G. Hautier, S. P. Ong, A. Jain, C. J. Moore and G. Ceder, *Phys. Rev. B*, 2012, **85**, 155208.
24. A. Márquez, M. J. Capitán, J. A. Odriozola and J. F. Sanz, *Int. J. Quantum Chem.*, 1994, **52**, 1329-1338.
25. Y. Feng and Z. Zhu, *Spectrochim. Acta, Part A*, 2019, **218**, 184-190.
26. B. Ruscic and D. H. Bross, *Active Thermochemical Tables (ATcT) based on ver. 1.122 of the Thermochemical Network (2016); available at ATcT.anl.gov*, https://atct.anl.gov, Accessed January 29, 2019.

27. A. Kramida, Y. Ralchenko and J. Reader, *NIST Atomic Spectra Database (ver 5.3), [Online]. Available: http://physics.nist.gov/asd [2018, April 1]*, National Institue of Standards and Technology, Gaithersburg, MD, 2018.
28. M. Olzmann and J. Troe, *Ber. Bunsen-Ges. Phys. Chem. Chem. Phys.*, 1992, **96**, 1327-1332.
29. W. J. Chesnavich and M. T. Bowers, *J. Chem. Phys.*, 1977, **66**, 2306-2315.
30. B. C. Sweeny, S. G. Ard, D. C. McDonald, O. Martinez, A. A. Viggiano and N. S. Shuman, *Chem. - Eur. J.*, 2017, **23**, 11780-11783.
31. H. Schwarz, *Chem. Phys. Lett.*, 2015, **629**, 91-101.
32. Y. Shiota and K. Yoshizawa, *J. Am. Chem. Soc.*, 2000, **122**, 12317-12326.
33. Z. C. Wang, N. Dietl, R. Kretschmer, J. B. Ma, T. Weiske, M. Schlangen and H. Schwarz, *Angew. Chem. Int. Ed.*, 2012, **51**, 3703-3707.
34. L. Yue, J. Li, S. Zhou, X. Sun, M. Schlangen, S. Shaik and H. Schwarz, *Angew. Chem. Int. Ed.*, 2017, **56**, 10219-10223.
35. L. Yue, N. Wang, S. Zhou, X. Sun, M. Schlangen and H. Schwarz, *Angew. Chem. Int. Ed.*, 2018, **57**, 14635-14639.
36. P. Hu, Z. Huang, Z. Amghouz, M. Makkee, F. Xu, F. Kapteijn, A. Dikhtiarenko, Y. Chen, X. Gu and X. Tang, *Angew. Chem. Int. Ed.*, 2014, **53**, 3418-3421.
37. L. Liu and A. Corma, *Chem. Rev.*, 2018, **118**, 4981-5079.
38. M. T. Darby, R. Réocreux, E. C. H. Sykes, A. Michaelides and M. Stamatakis, *ACS Catal.*, 2018, **8**, 5038-5050.

Graphical Abstract

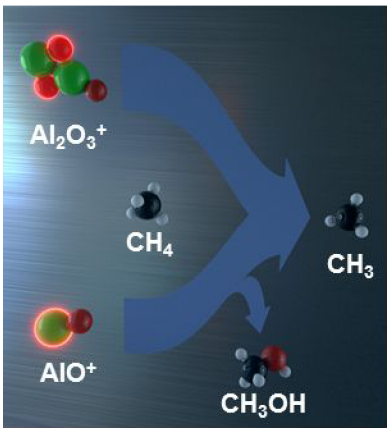

Alcohol for free? Aluminum can: Aluminum enables oxygen transfer to methane via a unique, barrierless formation of R-Al-MeOH. The key to completing conversion to methanol lies in the Al-MeOH bond strength, which may be tuned relative to other channels by controlling the acidity of the Al via electron-donating or withdrawing R groups.